



## The interfacial reactivity of arsenic species with green rust sulfate (GR<sub>SO4</sub>)



Jeffrey Paulo H. Perez<sup>a,b,\*</sup>, Helen M. Freeman<sup>a</sup>, Jan A. Schuessler<sup>a,1</sup>, Liane G. Benning<sup>a,b</sup>

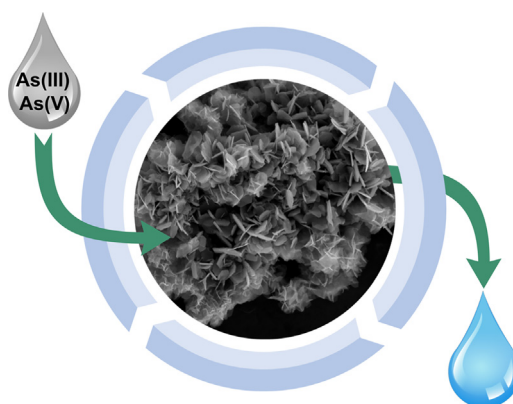
<sup>a</sup> GFZ German Research Center for Geosciences, Telegrafenberg, 14473 Potsdam, Germany

<sup>b</sup> Department of Earth Sciences, Free University of Berlin, 12249 Berlin, Germany

### HIGHLIGHTS

- GR<sub>SO4</sub> is among the best performing Fe-bearing minerals for As removal.
- Both pH and the presence of competing aqueous ions affect As removal efficiency.
- Long term experiments showed that GR<sub>SO4</sub> with As adsorbed onto its surface is stable for up to 90 days.
- High-resolution electron microscopy revealed that As is preferentially adsorbed at the GR particle edges.

### GRAPHICAL ABSTRACT



### ARTICLE INFO

#### Article history:

Received 14 June 2018

Received in revised form 1 August 2018

Accepted 12 August 2018

Available online 13 August 2018

Editor: José Virgilio Cruz

#### Keywords:

Arsenic  
Adsorption  
Green rust  
Groundwater treatment  
Iron (oxyhydr)oxide  
Layered double hydroxide

### ABSTRACT

Arsenic (As) contamination in groundwater is a significant health and environmental concern worldwide because of its wide distribution and toxicity. The fate and mobility of As is greatly influenced by its interaction with redox-active mineral phases, among which green rust (GR), an Fe<sup>II</sup>-Fe<sup>III</sup> layered double hydroxide mineral, plays a crucial role. However, the controlling parameters of As uptake by GR are not yet fully understood. To fill this gap, we determined the interfacial reactions between GR sulfate (GR<sub>SO4</sub>) and aqueous inorganic As(III) and As(V) through batch adsorption experiments, under environmentally-relevant groundwater conditions. Our data showed that, under anoxic conditions, GR<sub>SO4</sub> is a stable and effective mineral adsorbent for the removal of As(III) and As(V). At an initial concentration of 10 mg L<sup>-1</sup>, As(III) removal was higher at alkaline pH conditions (~95% removal at pH 9) while As(V) was more efficiently removed at near-neutral conditions (>99% at pH 7). The calculated maximum As adsorption capacities on GR<sub>SO4</sub> were 160 mg g<sup>-1</sup> (pH 8–9) for As(III) and 105 mg g<sup>-1</sup> (pH 7) for As(V). The presence of other common groundwater ions such as Mg<sup>2+</sup> and PO<sub>4</sub><sup>3-</sup> reduces the efficiency of As removal, especially at high ionic strengths. Long-term batch adsorption experiments (up to 90 days) revealed that As-interacted GR<sub>SO4</sub> remained stable, with no mineral transformation or release of adsorbed As species. Overall, our work shows that GR<sub>SO4</sub> is one of the most effective As adsorbents among iron (oxyhydr)oxide phases.

© 2018 Elsevier B.V. All rights reserved.

\* Corresponding author at: GFZ German Research Center for Geosciences, Telegrafenberg, 14473 Potsdam, Germany.

E-mail address: [jpperez@gfz-potsdam.de](mailto:jpperez@gfz-potsdam.de) (J.P.H. Perez).

<sup>1</sup> Current address: Thermo Fisher Scientific GmbH, 28199 Bremen, Germany.

## 1. Introduction

Elevated levels of dissolved arsenic (As) in ground- and drinking waters remain a significant global environmental and public health concern because of the wide-spread occurrence and distribution, as well as toxicity and mobility of As in the environment (Vaughan, 2006). In groundwaters, As is commonly present as inorganic oxyanions arsenite ( $\text{H}_3\text{As}^{\text{III}}\text{O}_3$ ) and arsenate ( $\text{H}_3\text{As}^{\text{V}}\text{O}_4$ ), with the former being the more toxic form (Hughes, 2002; Sharma and Sohn, 2009). Based on their acid dissociation constants, As(III) forms the neutral species  $\text{H}_3\text{As}^{\text{III}}\text{O}_3$  at moderately reducing conditions ( $\text{pK}_{\text{a}1,2,3} = 9.23, 12.13, 13.40$ ) while As(V) is present as  $\text{H}_2\text{As}^{\text{V}}\text{O}_4^-$  and  $\text{HAS}^{\text{V}}\text{O}_4^{2-}$  ( $\text{pK}_{\text{a}1,2,3} = 2.20, 6.97, 11.53$ ) in oxidized environments (Ferguson and Gavis, 1972; Inskip et al., 2002). However, it is important to note that the relatively slow redox transformation kinetics allows both As(III) and As(V) to persist under both anoxic and oxic conditions (Masscheleyn et al., 1991).

Green rust (GR) minerals are redox-active phases, which belong to the family of  $\text{Fe}^{\text{II}}\text{-Fe}^{\text{III}}$  layered-double hydroxides (LDHs). Their ability to treat or remove toxic metals from groundwater has been investigated (Usman et al., 2018), yet the fundamental adsorption properties or uptake capacities of metals on GR phases have still not been quantified. The high potential of GR as a material for groundwater remediation stems from its structural and redox properties. GR is composed of positively charged brucite-like layers of octahedrally coordinated  $\text{Fe}^{\text{II}}\text{-Fe}^{\text{III}}$  hydroxides that alternate with negatively charged interlayers of anions and water molecules, as well as monovalent cations (Christiansen et al., 2009). These brucite-like layers and interlayer regions are held together by hydrogen bonding and electrostatic forces. GR is typically represented by the general formula,  $[\text{Fe}^{\text{II}}_{(1-x)}\text{Fe}^{\text{III}}_x(\text{OH})_2]^{x+}[(x/n) \text{A}^{n-} \cdot m\text{H}_2\text{O}]^{x-}$ , where  $\text{A}^{n-}$  is the intercalated anion such as  $\text{Cl}^-$ ,  $\text{CO}_3^{2-}$  and  $\text{SO}_4^{2-}$ , and  $x$  is the molar fraction of  $\text{Fe}^{\text{III}}$ ,  $[\text{Fe}^{\text{III}}]/[\text{Fe}^{\text{total}}]$  (Géhin et al., 2002). These properties allow GR to remove toxic metal contaminants by adsorption (Jönsson and Sherman, 2008; Mitsunobu et al., 2009), reduction (Christiansen et al., 2011; O'Loughlin et al., 2003; Skovbjerg et al., 2006), interlayer intercalation (Refait et al., 2000), and substitution of structural Fe in the octahedral sheets (Ahmed et al., 2008; Refait et al., 1990).

Considering the worldwide health implications of As-contaminated ground- and drinking waters (World Health Organization, 2017), it is paramount that we understand the removal efficiency of As through interactions with various mineral substrates. There is an imminent challenge regarding the development, testing and validating the usefulness of adequate mineral phases that have high metal-specific uptake capacities, strong binding affinities and excellent stabilities. Adsorption-based technologies are promising groundwater clean-up strategies because of their facile implementation, relative cost-effectiveness and high removal efficiency (Leus et al., 2017). However, to optimize the efficiency of subsurface remediation strategies, the interactions between inorganic As species and the surfaces of redox-active minerals such as GR must be quantified in detail.

Su and Wilkin (2005) examined the interaction of As(III) and As(V) with synthetic green rust carbonate ( $\text{GR}_{\text{CO}_3}$ ) and monitored the changes in the aqueous phase. Their results showed that As(V) removal rates using  $\text{GR}_{\text{CO}_3}$  were higher compared to As(III) due to the higher affinity of iron (oxyhydr)oxides for As(V) than the more toxic As(III). The mechanism of adsorption of As species onto GR mineral phases (e.g.,  $\text{GR}_{\text{Cl}}$ ,  $\text{GR}_{\text{CO}_3}$ ,  $\text{GR}_{\text{SO}_4}$ ) has also been investigated previously using X-ray absorption spectroscopy (XAS) (Jönsson and Sherman, 2008; Randall et al., 2001; Wang et al., 2010). In these studies, As(III) and As(V) were found to both form bidentate binuclear ( $^2\text{C}$ ) and monodentate mononuclear ( $^1\text{V}$ ) inner-sphere complexes on the  $\text{FeO}_6$  octahedra at the edges of the GR crystal. However, the fundamental adsorption parameters (e.g., effects of pH, adsorbent loading, ionic strength, potentially competing ions), as well as the maximum uptake capacity and critical adsorption kinetics, necessary for understanding interactions between GR and As in groundwaters have never been evaluated in detail.

Herein, we aim to close this gap through an in-depth investigation on the interfacial interactions between freshly-precipitated green rust sulfate ( $\text{GR}_{\text{SO}_4}$ ) and aqueous inorganic As species. We evaluated the performance of  $\text{GR}_{\text{SO}_4}$  as an effective adsorbent for the removal of arsenite [As(III)] and arsenate [As(V)] by examining adsorption reactions as a function of pH, adsorbent loading, ionic strength, varying initial As concentrations, time and the presence of potentially interfering ions in groundwater. Our results reveal that  $\text{GR}_{\text{SO}_4}$  is a highly effective adsorbent for the removal of As species from groundwater.

## 2. Materials and methods

### 2.1. Mineral synthesis and characterization

GR with interlayer sulfate ( $\text{GR}_{\text{SO}_4}$ ) was synthesized in an anaerobic chamber (95%  $\text{N}_2$ , 5%  $\text{H}_2$ , Coy Laboratory Products, Inc.) at room temperature using the co-precipitation method (Géhin et al., 2002). In brief, separate Fe(II) (0.3 M) and Fe(III) (0.1 M) solutions were prepared from reagent grade  $(\text{NH}_4)_2\text{Fe}(\text{SO}_4)_2 \cdot 6\text{H}_2\text{O}$  and  $\text{Fe}_2(\text{SO}_4)_3$  salts (VWR) and deoxygenated Milli-Q water ( $\sim 18.2 \text{ M}\Omega \text{ cm}^{-1}$ ). GR synthesis was initiated by mixing the Fe(III) and Fe(II) solutions (pH  $\sim 2$ ) under constant stirring at 350 rpm. Subsequently, a 0.3 M NaOH solution was slowly titrated into the mixed  $\text{Fe}^{\text{II}}\text{-Fe}^{\text{III}}$  solution until the pH reached 8. Base addition resulted in the precipitation of a dark blue-green suspension, which was stirred and aged further for 1 h. The suspension was then washed with  $\text{O}_2$ -free Milli-Q water to remove excess solutes. The yield of the washed  $\text{GR}_{\text{SO}_4}$  slurry was determined based on the difference between the total Fe concentration of an aliquot of the suspension dissolved in 0.3 M  $\text{HNO}_3$  and the dissolved Fe concentration in the supernatant after filtration through a  $0.2\text{-}\mu\text{m}$  syringe filter. The Fe ion concentration was analyzed by inductively coupled plasma optical emission spectrometry (ICP-OES). Each batch of  $\text{GR}_{\text{SO}_4}$  slurry ( $\sim 8.2 \text{ g L}^{-1}$ ) was prepared fresh and kept in the anaerobic chamber adsorption experiments for a maximum of 24 h.

The solid  $\text{GR}_{\text{SO}_4}$  samples were analyzed by X-ray powder diffraction (XRD), nitrogen sorption, transmission electron microscopy (TEM), selected area electron diffraction (SAED), energy dispersive X-ray spectroscopy (EDX), electron energy-loss spectroscopy (EELS), high angle annular dark field scanning transmission electron microscopy (HAADF-STEM), X-ray photoelectron spectroscopy (XPS) and Mössbauer spectroscopy to determine their structure, particle sizes, morphologies, surface properties, as well as redox and full chemical composition. Detailed information on all phase characterizations can be found in the Supporting Information (Text S1).

### 2.2. Adsorption experiments

All batch adsorption experiments were carried out in triplicate at room temperature inside the anaerobic chamber using headspace crimp vials with the washed  $\text{GR}_{\text{SO}_4}$  suspensions ( $\text{S/L} = 4 \text{ g L}^{-1}$ ) reacted with  $10 \text{ mg L}^{-1}$  aqueous As(III) or As(V) solutions. The mixed samples were shaken at 250 rpm for 24 h followed by the separation of solids and supernatants by filtration through  $0.22\text{-}\mu\text{m}$  syringe filters. The obtained liquid phases were acidified (pH  $\sim 2$  with Merck Suprapur® grade  $\text{HNO}_3$ ) and stored at  $4^\circ\text{C}$  until analysis. The elemental composition of the liquid phases was determined following the method described in Schuessler et al. (2016) using an axial ICP-OES Varian 720ES. Full details of all tested parameters [e.g., varying pH (7 to 9), adsorbent loading (solid to solution ratio,  $\text{S/L}$  2 to  $6 \text{ g L}^{-1}$ ), ionic strength ( $\text{IS}^*$  0.5 to  $0.005 \text{ M}$ ), competing ions ( $\text{Ca}^{2+}$ ,  $\text{Mg}^{2+}$ ,  $\text{PO}_4^{3-}$ ) and time (5 min to 90 days)] for the batch adsorption experiments and analytical methods can be found in the Supporting Information (Text S1, Table S1).

### 2.3. Adsorption kinetics and isotherms

Kinetic rates of As adsorption were determined at pH 8 using an initial As concentration of  $10 \text{ mg L}^{-1}$  and an adsorbent loading of  $4 \text{ g L}^{-1}$ .

The mixtures were shaken for 5 min, 10 min, 15 min, 30 min, 1 h, 2 h, 4 h, 8 h, 16 h and 24 h after which the solids were separated from the supernatant and analyzed as described above. Adsorption isotherms were obtained at room temperature at pH 7 and 8–9 using an adsorbent loading of  $4 \text{ g L}^{-1}$ , initial As concentrations up to  $1000 \text{ mg L}^{-1}$  and contact time of 24 h. The obtained equilibrium adsorption data were fitted to the Langmuir and Freundlich isotherm models (Limousin et al., 2007).

### 3. Results and discussion

#### 3.1. Synthesis and characterization of $\text{GR}_{\text{SO}_4}$

The morphology, size and chemical composition of the synthesized  $\text{GR}_{\text{SO}_4}$  particles were characterized by TEM imaging and analytical spectroscopy. The micrographs (Fig. 1a) of the synthesized material revealed a well-defined hexagonal plate-like morphology typical of  $\text{GR}_{\text{SO}_4}$  (Géhin et al., 2002). The diameter of particles varied between 50 and 500 nm while the estimated thickness of the particles calculated by the log-ratio (relative) method (Malis et al., 1988) from the low loss EEL spectra was around 16 to 20 nm. The SAED pattern (Fig. 1a inset) shows the distinctive hexagonal *c*-axis spot pattern of a single crystal  $\text{GR}_{\text{SO}_4}$  (Ahmed et al., 2010). The elemental composition (Table S2), which was calculated from the EDX spectra, is comparable to the theoretical values based on the chemical formula,  $\text{Fe}^{\text{II}}_4\text{Fe}^{\text{III}}_2(\text{OH})_{12}\text{SO}_4 \cdot 8\text{H}_2\text{O}$  (Simon et al., 2003). The mineralogy of the freshly-precipitated material was confirmed through XRD patterns (Fig. S1) to be pure  $\text{GR}_{\text{SO}_4}$  as evidenced through the typical sharp and symmetric basal (00 $l$ ) reflections corresponding to the interlayer distances between the  $\text{Fe}^{\text{II}}$ - $\text{Fe}^{\text{III}}$  octahedral hydroxide sheets (Simon et al., 2003). No other iron (oxyhydr)oxide phases were identified in the freshly-precipitated  $\text{GR}_{\text{SO}_4}$  samples.

The oxidation state of Fe can be determined by the EELS  $\text{Fe L}_3$ -edge position and shape, where octahedrally coordinated  $\text{Fe(III)}$  has a peak energy  $\sim 1.8 \text{ eV}$  higher than octahedrally coordinated  $\text{Fe(II)}$  (Brown et al., 2017). Separate peaks attributed to  $\text{Fe}^{2+}$  (709 eV) and  $\text{Fe}^{3+}$  (710.8 eV) within the primary  $\text{L}_3$  peak are resolvable when EEL spectra are acquired at higher resolution EELS ( $< 0.3 \text{ eV}$ ). Using the EELS resolution of the microscope used for this work (0.8 eV), the  $\text{Fe(II)/Fe(III)}$  ratio was estimated by comparing our experimental spectra to reference spectra collected under the same conditions. Theoretical spectra were calculated by stoichiometrically combining the intensity-normalized spectra of the Fe standards for hedenbergite (octahedrally coordinated  $\text{Fe}^{2+}$ ) and hematite (octahedrally coordinated  $\text{Fe}^{3+}$ ). This resulted in a theoretical spectrum for  $\text{GR}_{\text{SO}_4}$  (where  $\text{Fe(II)/Fe(III)} = 2$ ) which allowed for the direct comparison between the  $\text{Fe L}_3$  peak shape and position in our sample and the theoretical spectrum (blue line in Fig. 1b;

Fig. S2a). This revealed that the shape of the  $\text{Fe L}_3$ -edge for the  $\text{GR}_{\text{SO}_4}$  sample matched the linear reference fit for a  $\text{Fe(II)/Fe(III)}$  ratio of 2, with minor differences. This is evidenced by the changes in shape and position of the  $\text{L}_3$  peak in the theoretical spectrum as the GR composition becomes more  $\text{Fe(III)}$ -rich. This is also clearly shown in Fig. S2, where the theoretical spectra for  $\text{Fe(II)/Fe(III)}$  ratios from 1 to 0.2, and the residual of each fit are shown. These results suggest that our sample had a  $\text{Fe(II)/Fe(III)}$  ratio corresponding to 2.

The surface chemistry of the synthesized  $\text{GR}_{\text{SO}_4}$  was analyzed by XPS and the wide scan spectrum (Fig. S3) revealed photoelectron peaks of Fe 2p, O 1s and S 2p at binding energies of 710.7, 531.9 and 168.8 eV, respectively. The Fe 2p $_{1/2}$  and 2p $_{2/3}$  photoelectron peaks (Fig. 2a) were observed at 724.0 and 710.7 eV, respectively. The value of the Fe 2p $_{2/3}$  peak maxima was shifted to slightly higher binding energy compared to a GR with interlayer carbonate ( $\text{GR}_{\text{CO}_3}$ , 709.4 eV), which also has an  $\text{Fe(II)/Fe(III)}$  ratio of 2.0 (Mullet et al., 2008). This indicates a slightly higher  $\text{Fe(III)}$  content in our synthesized  $\text{GR}_{\text{SO}_4}$ . However, the presence of a characteristic Fe(II) satellite peak at 726.7 eV and a Fe(III) satellite peak at 731.0 eV confirmed the presence of both Fe(II) and Fe(III) in our sample at the desired ratio of 2. The peak shape and positions of the Fe 2p $_{1/2}$  and 2p $_{2/3}$  photoelectron peaks were also similar to previously reported XPS spectra for  $\text{GR}_{\text{SO}_4}$  (Nedel et al., 2010). Furthermore, the relative contributions of the deconvoluted O 1s peaks at 530.2, 531.8 and 532.6 eV (Fig. 2b) that were assigned to Fe-O, O-H and adsorbed water (Table S3), respectively, were in agreement with values obtained by Mullet et al. (2008). The S 2p doublet (Fig. 2c) at 168.8 eV confirmed the presence of  $\text{SO}_4^{2-}$  in the interlayer region.

The iron chemistry of the synthesized  $\text{GR}_{\text{SO}_4}$  was characterized by Mössbauer spectroscopy which revealed two apparent doublets (Fig. S3), but with a certain line broadening of the outer doublet and a slight asymmetry of its line shape. An improved fit shown in Fig. 2d was obtained by using three doublets  $D_1$ ,  $D_2$  and  $D_3$  (hyperfine parameters, see Table S4). In this fit, doublets  $D_1$  and  $D_2$  correspond to high spin Fe(II) cations in the brucite-like octahedral sheets while doublet  $D_3$  corresponds to high spin Fe(III) cations (Géhin et al., 2002). The relative areas of the doublets in the Mössbauer spectrum allowed us to calculate an  $\text{Fe(II)/Fe(III)}$  ratio in the  $\text{GR}_{\text{SO}_4}$  sample of 2.09, which is in agreement with the ratio of 2 from our EELS data (Fig. 1b, Fig. S2), as well as literature data (Géhin et al., 2002; Simon et al., 2003). However, it should be noted that the Mössbauer spectra for  $\text{GR}_{\text{SO}_4}$  reported in literature are usually fitted with one Fe(II) doublet (Fig. S3, Table S5) instead of two doublets (Fig. 2d). It is worth noting nevertheless, that in our  $\text{GR}_{\text{SO}_4}$ , the two doublets  $D_1$  and  $D_2$  revealed the same isomer shift, but these differed somewhat in their quadrupole splittings ( $\Delta E_Q$ ), thereby suggesting the presence of two inequivalent Fe(II) sites. The component with the largest  $\Delta E_Q$  was attributed to Fe(II) ions far away from the

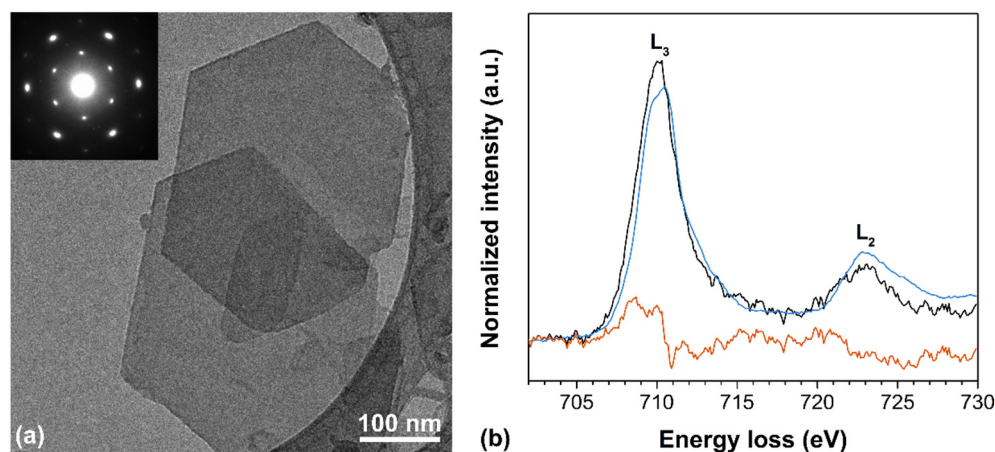


**Fig. 1.** (a) TEM image of  $\text{GR}_{\text{SO}_4}$  with SAED pattern of a single particle in inset. (b) Fe  $\text{L}_{2,3}$ -edge EEL spectrum of  $\text{GR}_{\text{SO}_4}$  sample (black), linear reference fit (blue) and residual spectrum (orange). (For interpretation of the references to colour in this figure legend, the reader is referred to the web version of this article.)

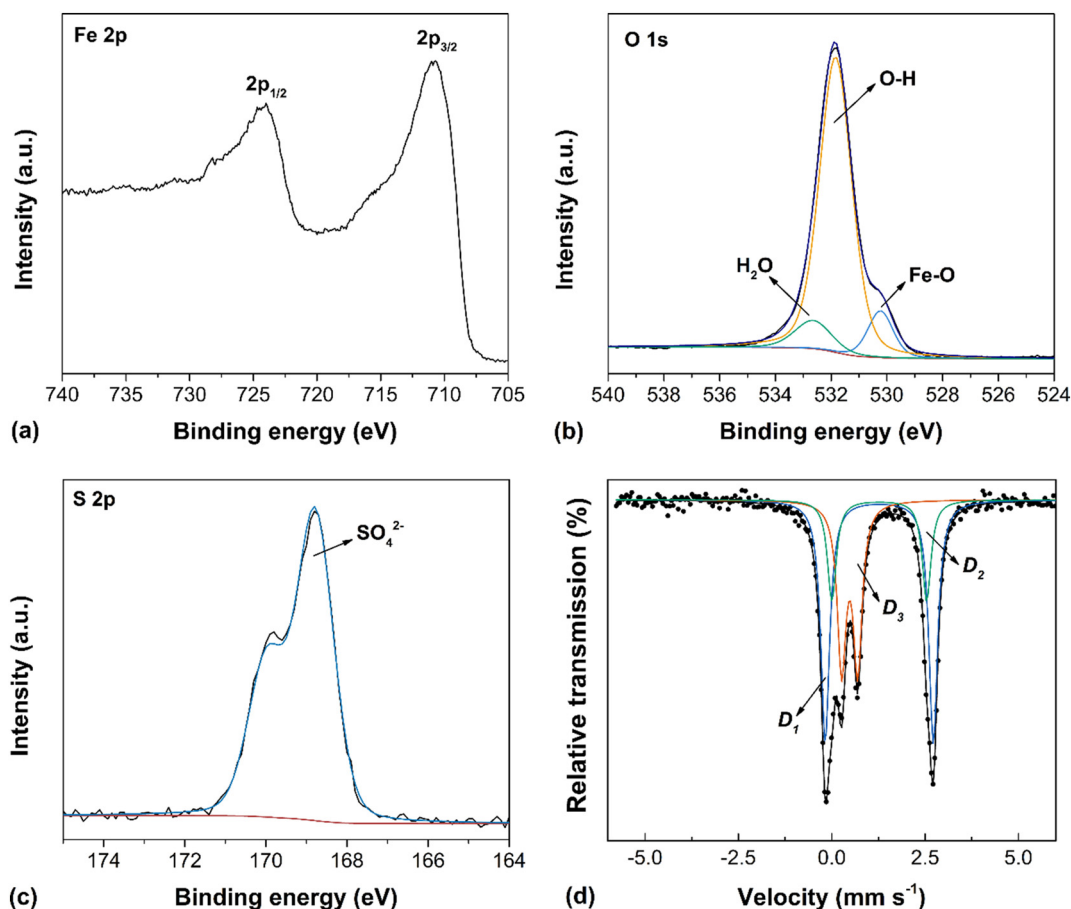


Fig. 2. (a–c) High resolution XPS spectra of  $GR_{SO_4}$ : (a) Fe 2p, (b) O 1s and (c) S 2p spectra. (d)  $^{57}Fe$  Mössbauer spectrum of  $GR_{SO_4}$  recorded at 20 K and fitted with three doublets.

anions (Génin and Ruby, 2004), whereas the presence of a component with smaller  $\Delta E_Q$  suggested the presence of Fe(II) sites containing anions in their environment. Such components have been previously observed in Mössbauer spectra of GR samples with other interlayer anions like carbonate or chloride but not for sulfate (Génin and Ruby, 2004).

### 3.2. Influence of environmental parameters on As removal

The effect of pH, adsorbent loading (solid to liquid ratio, S/L), ionic strength ( $IS^*$ ) and the presence of other potentially interfering aqueous groundwater ions were investigated to determine their influence on the adsorption of As species on  $GR_{SO_4}$ . The removal efficiencies of  $GR_{SO_4}$  for As(III) and As(V) at an initial concentration of  $10 \text{ mg L}^{-1}$  and under the above mentioned varying conditions are shown in Fig. 3.

At all pH values tested, the As(V) removal efficiencies (Fig. 3a) were higher compared to As(III). This is likely because of the higher adsorption affinity of the pentavalent species on iron (oxyhydro)oxide surfaces. No significant differences in As(V) removal efficiencies between pH 7, 8 and 9 were observed (i.e. within analytical uncertainties <2%). Although there were no significant differences in removal efficiencies,  $GR_{SO_4}$  can effectively remove As(V) at a relatively wide range of pH conditions that can be found in contaminated groundwaters (Nickson et al., 2000; Smedley and Kinniburgh, 2002; Zahid et al., 2008). On the contrary, the removal efficiency of As(III) by  $GR_{SO_4}$  was significantly affected by pH, which is the opposite of what was expected. With pH, As(III) removal efficiency ( $50.1 \pm 1.5\%$  at pH 7) increased by >30% at pH 8 ( $83.7 \pm 0.9\%$ ) and another 10% increase was measured at pH 9 ( $94.6 \pm 0.1\%$ ). Such surface polymerization of As(III) complexes has been previously suggested for  $GR_{Cl}$  and  $GR_{CO_3}$  by XAS analysis (Ona-Nguema et al., 2009; Wang et al., 2010). Usually, the influence of pH

on As adsorption by iron (oxy)hydroxides is controlled by two factors: (1) the speciation of the As in solution and (2) the point of zero charge (PZC) of the adsorbent. Over the pH range tested here, As(III) will mostly exist as  $H_3AsO_3^0$  and  $H_2AsO_3^-$  species while As(V) is present as  $H_2AsO_4^-$  and  $HAso_4^{2-}$  species (Jain et al., 1999). For  $GR_{SO_4}$  with a PZC of 8.3 (Guilbaud et al., 2013), the net surface charges will be negative at  $pH > 8.3$  and positive at  $pH < 8.3$ . As a result of electrostatic repulsion caused by similar negative charges, one would expect the removal of both As(III) and As(V) species to decrease as the pH is increased from 8 to 9, which was not observed in our study. Particularly, for As(III), the biggest increase in removal was observed between pH 7 and 8 with a lesser change between 8 and 9 (Fig. 3a). Similar trends have been observed for As interacted with  $GR_{CO_3}$  (Jönsson and Sherman, 2008) and ferrihydrite (Jain et al., 1999; Raven et al., 1998). An increased As(III) adsorption at higher pH can be attributed to the possible formation of multi-nuclear complexes on the surfaces of  $GR_{SO_4}$ .

With increased adsorbent loading from  $2$  to  $4 \text{ g L}^{-1}$ , the removal efficiency of As(III) also increased by  $\sim 15\%$  from  $34.6 \pm 2.7$  to  $50.1 \pm 1.5\%$  (Fig. 3b). This increase was caused by the larger number of active surface sites available for As(III) complexes (Asere et al., 2017). However, with further increase in loading to  $6 \text{ g L}^{-1}$ , the efficiency decreased to  $39.2 \pm 6.2\%$ . In the case of As(V), no significant differences (<0.3% relative) in removal efficiencies were observed among the adsorbent loadings tested (Fig. 3b).

The removal efficiencies for both As species decreased with increasing ionic strength,  $IS^*$  (Fig. 3c). For As(V), this decrease was only about 10% (from  $>99.8$  to  $90.1 \pm 0.4\%$ ) as ionic strength increased from 0.005 to 0.5 M. On the other hand, this inhibitory effect was more pronounced for As(III) where the removal efficiency decreased from  $58.9 \pm 3.2\%$  at an ionic strength of 0.005 M to  $37.8 \pm 0.4\%$  at an ionic strength of 0.5 M, although the overall removal was lower compared to As(V).

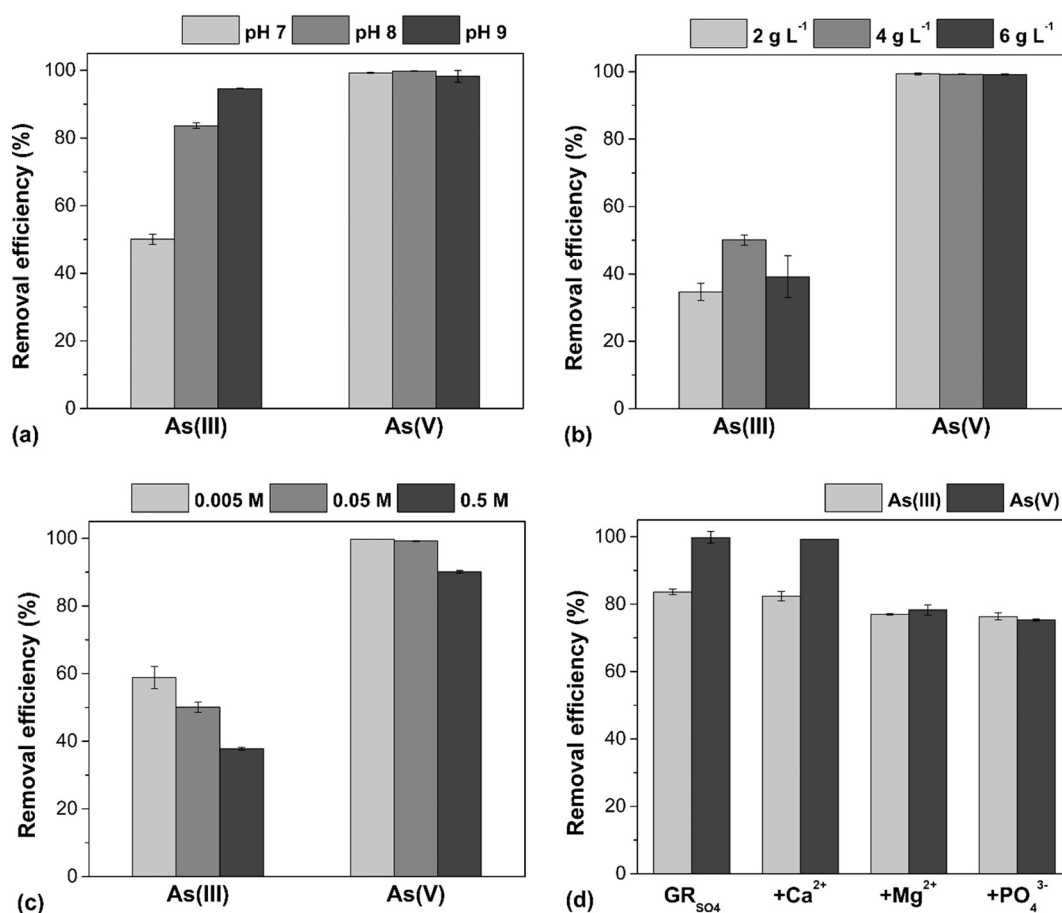


**Fig. 3.** Removal of 10 mg L<sup>-1</sup> As(III) and As(V) upon interaction with GR<sub>SO4</sub> after 24 h as a function of: (a) pH (S/L = 4 g L<sup>-1</sup>, IS\* = 0.05 M), (b) adsorbent loading, S/L (pH 7, IS\* = 0.05 M), (c) ionic strength, IS\* (pH 7, S/L = 4 g L<sup>-1</sup>) and (d) presence of competing groundwater ions (at pH 8 and IS\* = 0.05 M): pure GR<sub>SO4</sub> (no competing ion), Ca<sup>2+</sup> (100 mg L<sup>-1</sup>), Mg<sup>2+</sup> (50 mg L<sup>-1</sup>) or PO<sub>4</sub><sup>3-</sup> (10 mg L<sup>-1</sup>). Error bars represent standard deviations of triplicate experiments (<5% relative). Note: IS\* here is defined as the ionic strength based on a 10× and 100× dilution from the initial 0.5 M IS of the GR<sub>SO4</sub> suspension (further details, see in Supporting Information Text S1).

The decrease in As removal at higher IS\* can be caused by the decrease in available surface sites of GR<sub>SO4</sub>. This results from potential aggregation of GR<sub>SO4</sub> particles due to disturbances in the electrostatic double layer (Shiple et al., 2009). Although the presence of ionic species in the supernatant can also decrease the removal efficiency, the dissolved solutes in our experiments (e.g., Fe<sup>2+</sup>, NH<sub>4</sub><sup>+</sup>, Na<sup>+</sup>, Cl<sup>-</sup> and SO<sub>4</sub><sup>2-</sup> ions) have been shown to have little or no effect on As adsorption (Asere et al., 2017; Guo and Chen, 2005; Gupta et al., 2009).

Common aqueous groundwater ions can compete for the available active surface sites on GR<sub>SO4</sub> (Folens et al., 2016; Leus et al., 2018). We tested the effect of relevant dissolved potentially interfering ions in the water matrix through competitive adsorption experiments with Ca<sup>2+</sup> (100 mg L<sup>-1</sup>), Mg<sup>2+</sup> (50 mg L<sup>-1</sup>) or PO<sub>4</sub><sup>3-</sup> (10 mg L<sup>-1</sup>) and As (10 mg L<sup>-1</sup>) to the GR<sub>SO4</sub> suspension at pH 8. The concentrations of the competing ions were chosen based on the average aqueous ion concentrations in As-contaminated groundwaters in Bangladesh and West Bengal, India (Nickson et al., 2000; Zahid et al., 2008) and mining-contaminated groundwater sites (Smedley and Kinniburgh, 2002; Williams et al., 1996). The comparison (Fig. 3d) revealed no significant change in the removal of As(III) and As(V) resulting from the presence of Ca<sup>2+</sup> ions. On the other hand, the presence of Mg<sup>2+</sup> ions decreased the removal efficiency by 6.7 ± 1.0% for As(III) and 21.5 ± 2.1% for As(V) compared to the Mg<sup>2+</sup> free system. However, analysis of the liquid phases by ICP-OES revealed that Mg<sup>2+</sup> was not adsorbed on GR<sub>SO4</sub>, but remained solvated in the supernatant. This decrease in As removal can be caused by the high ionic potential of Mg<sup>2+</sup>, allowing it to be solvated by water molecules (Lightstone et al., 2001) and resulting in the formation of outer-sphere hydrated Mg<sup>2+</sup> complexes. Such aqueous

complexes could potentially reduce the accessibility of active surface sites of GR<sub>SO4</sub> for As adsorption. The presence of PO<sub>4</sub><sup>3-</sup> ions also resulted in the inhibition of As adsorption, where the removal efficiency for As(III) and As(V) decreased by 7.3 ± 1.3 and 24.5 ± 1.8%, respectively. Phosphate, with a tetrahedral molecular geometry analogous to the structure of AsO<sub>4</sub><sup>3-</sup>, can also form complexes in the same lateral (010) and (100) GR surfaces sites where As complexes bind (Bocher et al., 2004). This can result in a competition between PO<sub>4</sub><sup>3-</sup> and As species on the available GR<sub>SO4</sub> binding sites, thereby explaining the reduced As removal efficiency. Remarkably, the phosphate removal efficiency was >90% for both the As(III) and As(V) competitive adsorption experiments. This likely results from the higher affinity of iron (oxyhydr)oxides for phosphate compared to As, as indicated by its higher adsorption equilibrium constant (Roberts et al., 2004), and the slow exchange of initially adsorbed phosphate on the GR<sub>SO4</sub> surface sites with the competing As species (Hongshao and Stanforth, 2001).

### 3.3. Adsorption kinetics

The rate of As removal over 24 h was determined at pH 8 by measuring the adsorption kinetics in batch experiments at initial As concentration of 10 mg L<sup>-1</sup> As(III) or As(V), S/L of 4 g L<sup>-1</sup> and an ionic strength of 0.05 M. After fitting the kinetic data with various adsorption models, the best fit ( $R^2 > 0.9999$ ) resulted from the pseudo-2nd order kinetic model (Ho, 2006). The linearized plots for the pseudo-2nd order kinetic model are shown in Fig. 4. The calculated adsorption rate constants ( $k_2$ ; Table S6) revealed that the uptake of both As species was very fast. Full adsorption (>99% removal) of As(V) was achieved within 30 min

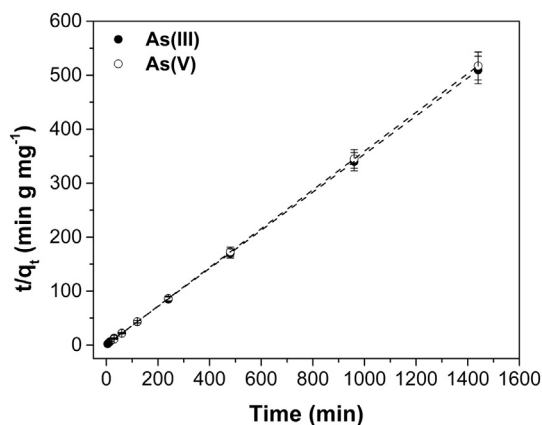


**Fig. 4.** Pseudo-2nd order kinetic data and model fits for the adsorption of As species on  $GR_{SO_4}$ . Initial concentration is  $10 \text{ mg L}^{-1}$  at pH 8, S/L ratio of  $4 \text{ g L}^{-1}$  and  $IS^*$  of 0.05 M. Error bars represent analytical uncertainty (<5% relative) based on replicate measurements of QC solutions analyzed together with the samples (Table S1).

of contact with  $GR_{SO_4}$ , while As(III) reached equilibrium after 4 h. The more rapid removal of As(V) was caused by the stronger binding affinity of pentavalent As over the trivalent As species to iron (oxyhydr)oxides (Roberts et al., 2004). These fast adsorption uptake rates show that  $GR_{SO_4}$  can efficiently remove As(III) and As(V) within a short time.

### 3.4. Long-term batch adsorption experiments

At an initial As concentration of  $10 \text{ mg L}^{-1}$ ,  $GR_{SO_4}$  remained stable during the course of the 90-day monitoring of batch adsorption experiments. No other iron (oxyhydr)oxide mineral phases were identified in XRD patterns of these long-term equilibrated and As-interacted samples (Fig. 5a). The TEM images and SAED patterns (Fig. 5b) also showed that the  $GR_{SO_4}$  particles in the 90-day long interacted samples maintained their well-defined thin hexagonal plate-like morphology and crystal structure. These observations were also confirmed by the fact that the long-term monitoring of aqueous As in the supernatant (Fig. S6) revealed that the initial adsorbed As was not released back into the aqueous phase. Previous studies have shown that adsorbed As can slow down or inhibit the transformation of GR minerals to other iron (oxyhydr)oxides such as magnetite (Su and Wilkin, 2005; Wang et al., 2014), which explains the stability of the As-interacted  $GR_{SO_4}$  even after 90 days in our study. In addition, our results are also consistent with long-term batch experiments of Su and Wilkin (2005), who showed that As-interacted  $GR_{CO_3}$  remained stable for up to 60 days.

### 3.5. Adsorption isotherms and mechanism

The As adsorption isotherms at all tested pH values are shown in Fig. 6. Equilibrium adsorption data were fitted to Langmuir and Freundlich isotherm models and the calculated fitting parameters for both models are shown in Table S7. Based on the fitting, the adsorption of As species on  $GR_{SO_4}$  is best described using the Langmuir model, indicating a homogeneous monolayer binding of As surface complexes at the solid/water interface (Leus et al., 2017). Using the Langmuir adsorption model, we determined the maximum As adsorption capacities for both As species onto  $GR_{SO_4}$  (Table 1). At alkaline pH, the maximum adsorption capacity of As(III) was 2.2 times higher than the value at neutral pH, while As(V) had 1.5 times higher maximum adsorption capacity at pH 7 compared to pH 8–9.

The spatial distribution of the adsorbed As(III) on the GR particles, at an initial concentration of  $500 \text{ mg L}^{-1}$ , was examined using HAADF-STEM imaging coupled with EDX mapping (Fig. 7). The EDX elemental map (Fig. 7d) and associated intensity profile (Fig. 7g) show that higher concentrations of As can be found near the GR particle edges (ca. two

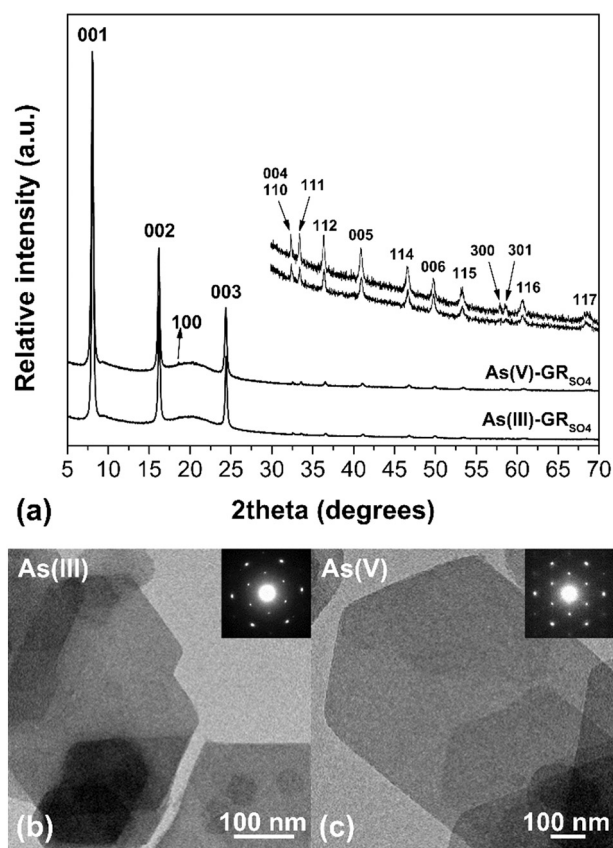


**Fig. 5.** (a) XRD patterns and (b–c) TEM images (inset: SAED pattern)  $GR_{SO_4}$  interacted with  $10 \text{ mg L}^{-1}$  As(III) and As(V) after 90 days. XRD peaks of  $GR_{SO_4}$  were assigned based on published diffraction data (Simon et al., 2003). The broad amorphous hump at  $\sim 20^\circ$   $2\theta$  comes from the XRD sample holder.

times higher than the (001) GR surface). In addition, the HAADF-STEM image (Fig. 7a) alone shows increased intensity at the GR particle edges which we interpret to be associated with increased As concentration. These results, combined with the adsorption isotherm results, strengthen previous findings that suggested that As(III) and As(V) form monodentate mononuclear ( $^1V$ ) and bidentate binuclear ( $^2C$ ) inner-sphere complexes on the GR particle edges (Jönsson and Sherman, 2008; Wang et al., 2010). However, the maximum adsorption capacity for As(III) determined in the current study could also indicate that surface complexation may not be limited to the  $GR_{SO_4}$  particle edges but, as mentioned before, may also result from the presence of multi-nuclear arsenite complexes (Ona-Nguema et al., 2009; Wang et al., 2010).

In addition to surface complexation, previous studies with selenate have shown that tetrahedral oxyanions (e.g.,  $SeO_4^{2-}$ ) can also be removed by GR phases by interlayer intercalation (Refaat et al., 2000). In our study, intercalation of As(III) and As(V) in the interlayer region of GR would have resulted in changes in the basal spacing since the ionic radius of  $AsO_3^{3-}$  (2.11 Å) and  $AsO_4^{3-}$  (2.48 Å) are different to that of  $SO_4^{2-}$  (2.30 Å) (Goh et al., 2008). However, XRD patterns of  $GR_{SO_4}$  interacted with As(III) and As(V) at  $10 \text{ mg L}^{-1}$  (Fig. 5a) and  $500 \text{ mg L}^{-1}$  (Fig. S7) did not exhibit shifts in the basal (001) reflections ( $\sim 10.93$  Å) to accommodate such intercalations. The intercalation of As(III) and As(V) in our study, might have been inhibited because  $SO_4^{2-}$  cannot be readily exchanged in layered double hydroxides (de Roy et al., 2001; Miyata, 1983).

### 3.6. Environmental significance of GR mineral phases in As-contaminated environments

Using the adsorption isotherm modelling data, we compared the calculated adsorption capacities for As species on  $GR_{SO_4}$  and with literature

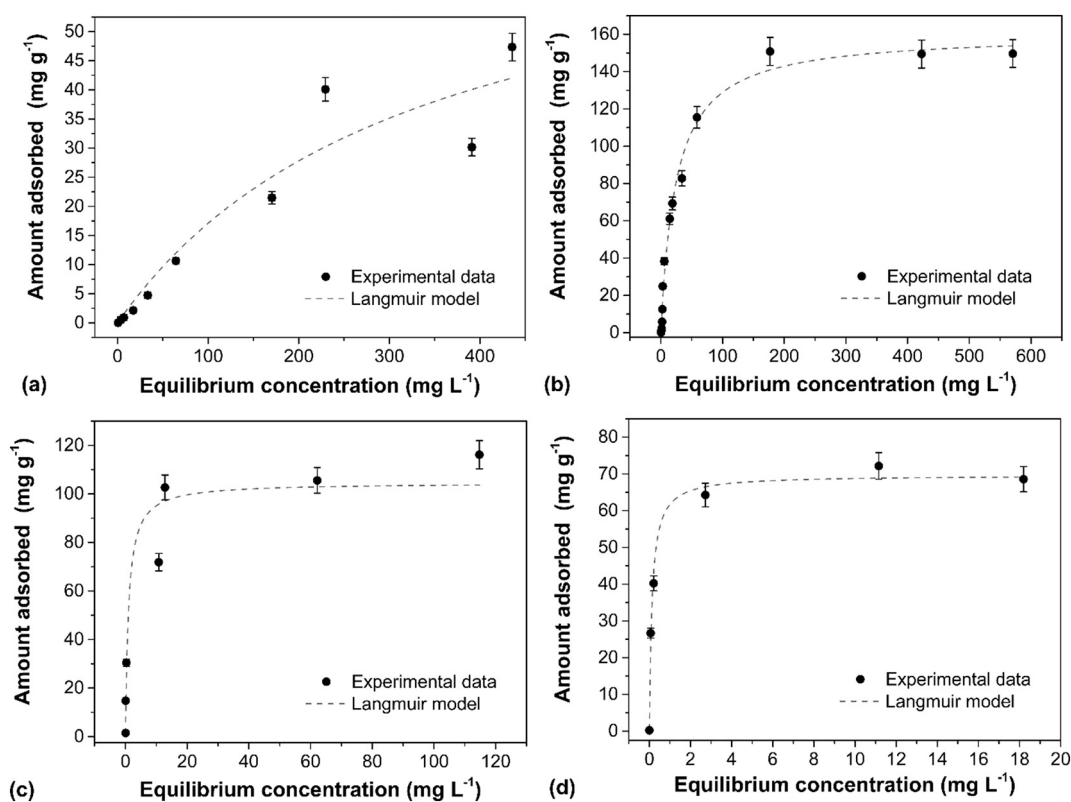


**Fig. 6.** Langmuir adsorption isotherms of As species on  $GR_{SO_4}$ . (a–b) Adsorption of As(III) at pH 7 and 8–9, respectively. (c–d) Adsorption of As(V) at pH 7 and 8–9, respectively. Error bars represent analytical uncertainty (<5% relative) based on replicate measurements of QC solutions analyzed together with the samples (Table S1).

data for all described iron (oxyhydr)oxides, oxyhydroxysulfates and sulfides, which have also been evaluated for their efficiency as mineral substrate for the treatment of As contaminated groundwater resources (Table 1).

Our data show clearly that  $GR_{SO_4}$  is among the most effective adsorbents among all the phases listed in Table 1. This finding has important implications for the fate and mobility of As in anoxic groundwaters where  $GR_{SO_4}$  exists. To the best of our knowledge, this is the first study to report the adsorption isotherms of As(III) and As(V) for  $GR_{SO_4}$ , as well as the in-depth examination of critical adsorption parameters for As removal. We have shown that at circum-neutral and slightly alkaline pH conditions,  $GR_{SO_4}$  can efficiently adsorb large amounts of As (III) and As(V), making  $GR_{SO_4}$  one of the best performing iron-bearing

mineral phases in terms of As adsorption. For As(III) at slightly alkaline pH,  $GR_{SO_4}$  is only outperformed by ferrihydrite (Table 1 entry 5) and schwertmannite (Table 1 entry 6) (Davidson et al., 2008). Ferrihydrite and schwertmannite are poorly ordered, highly reactive and thermodynamically metastable iron-bearing mineral phases which can transform at ambient conditions to more thermodynamically stable crystalline iron (oxyhydr)oxides such as goethite and hematite, fast at alkaline conditions but slow at near-neutral pH values (Brinza et al., 2015; Burton et al., 2008; Davidson et al., 2008; Vu et al., 2013; Yee et al., 2006). Moreover, comparing our data with other Fe-bearing phases (Table 1) shows that among mixed-valent and redox-active iron (oxyhydr)oxides and sulfides,  $GR_{SO_4}$  exhibits an unprecedented As(III) uptake and also remains stable for long time periods. Even compared

**Table 1**  
Comparison of As adsorption capacities of  $GR_{SO_4}$  with common iron (oxyhydr)oxides, oxyhydroxysulfates and sulfides.

Entry no.	Adsorbent	Particle size (nm)	Surface area ( $m^2 g^{-1}$ ) <sup>a</sup>	Tested pH	Adsorption capacity ( $mg g^{-1}$ )		Reference
					As(III)	As(V)	
1	Goethite	–	39	9	22.0	4.0	Lenoble et al. (2002)
2	Hematite	5	162	7	95.0	47.0	Tang et al. (2011)
3	Maghemite	7–12	169	–	67.0	95.4	Lin et al. (2012)
4	Magnetite	12	99	8	134.9	172.3	Yean et al. (2005)
5	Ferrihydrite	–	202	5	552.9	222.1	Raven et al. (1998)
6	Schwertmannite	–	280 <sup>b</sup>	9	280.4	166.5	Burton et al. (2009)
7	Mackinawite	2	350	7	9.7	32.2	Wolthers et al. (2005)
8	Troilite	–	3	7	17.3	–	Bostick and Fendorf (2003)
9	Pyrite	–	41	7	1.0	–	Bostick and Fendorf (2003)
10	$GR_{CO_3}$	100–300	–	7.5	123.0	–	Su and Wilkin (2005)
				10.5	43.8	6.91	Su and Wilkin (2005)
11	$GR_{SO_4}$	50–500	25 <sup>c</sup>	7	74.0	104.5	This work
				8–9	160.3	69.6	This work

<sup>a</sup> Specific surface area determined by the Brunauer–Emmett–Teller (BET) model.

<sup>b</sup> Estimated from Davidson et al. (2008).

<sup>c</sup> Measured nitrogen sorption isotherm can be found in Fig. S5.

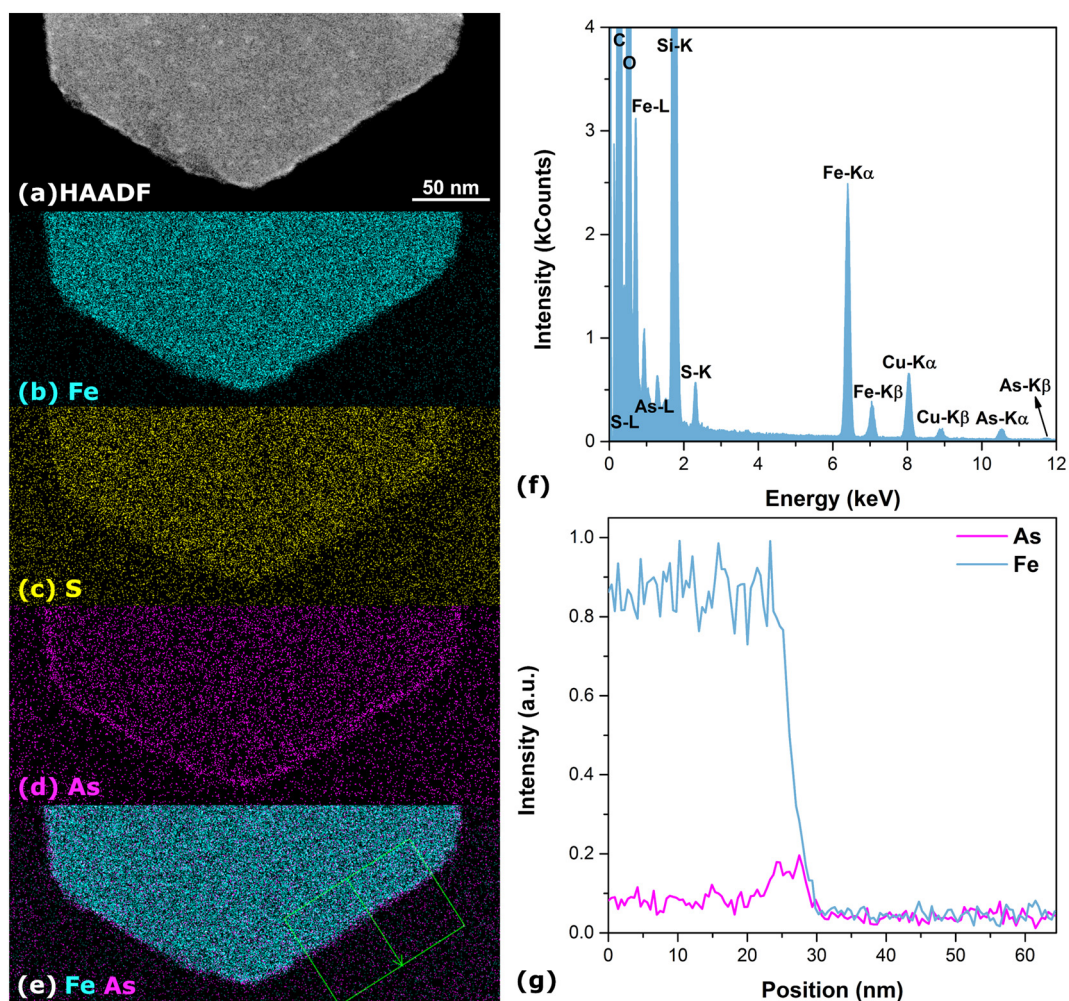


**Fig. 7.** (a) HAADF-STEM overview of  $GR_{SO_4}$  interacted with  $500 \text{ mg L}^{-1}$  of As(III) and the corresponding (b) EDX elemental maps for (b) Fe (light blue), (c) S (yellow), (d) As (magenta) and (e) combined Fe and As. (f) The EDX spectrum of (a). The Si signal comes from the use of headdress crimp vials while C and Cu peaks come from the TEM grid. (g) The EDX signal intensity profile shows the change in concentration of Fe and As along the integrated line drawn across the marked area in green (e). (For interpretation of the references to colour in this figure legend, the reader is referred to the web version of this article.)

to magnetite (Table 1 entry 4) and iron sulfides (e.g., troilite, pyrite; Table 1 entries 7–9) that are crystalline and highly stable in reduced environments, our  $GR_{SO_4}$  showed higher adsorption capacities. This exceptional As adsorption capacity makes  $GR_{SO_4}$  a novel and potentially highly environmentally-relevant mineral substrate for As sequestration in near-neutral pH and reduced to slightly oxidized groundwater systems.

Previous studies have shown that GR phases can oxidize As(III) to As(V) (Su and Puls, 2004; Su and Wilkin, 2005). Although not investigated in this study, possible redox transformation can heavily impact the toxicity and mobility of As in soils and groundwaters. As(III) oxidation by GR mineral phases would be a favorable process as it would result in a less toxic and less mobile As(V) species (Vaughan, 2006). On the other hand, reduction of As(V) to the far more toxic As(III) and the potential re-release into groundwaters because of the lower affinity of As(III) for ferric iron (oxyhydr)oxides would be far more damaging (Roberts et al., 2004). Further studies are needed to confirm the potential of As(III) oxidation in the presence of GR and to determine the geochemical and thermodynamic driving forces in this reaction.

As for redox-active mineral adsorbents, arsenic can still be released from  $GR_{SO_4}$  since its sequestration is highly dependent on pH conditions and redox environment. Sudden changes in pH or Eh of the system may cause potential release of surface immobilized As species back into the groundwater either by dissolution or redox-change driven transformation of GR phases (Cundy et al., 2008). Iron mineral phases such as

goethite and magnetite, which are common transformation end-products of GR, are, however, far less reactive and effective mineral substrates for As sequestration (Table 1), which can lead to remobilization of As in groundwaters.

#### 4. Conclusions

In this work, we investigated the interfacial reactivity between  $GR_{SO_4}$  and As species. An extensive batch adsorption study was performed to examine the influence of various critical environmental parameters such as initial concentration, pH, adsorbent loading, ionic strength and presence of potentially interfering ions on As removal. We have successfully demonstrated that  $GR_{SO_4}$  is an effective and stable As(III) and As(V) mineral adsorbent compared to other iron (oxyhydr) oxide phases.  $GR_{SO_4}$  demonstrated remarkable maximum adsorption capacities for As(III) and As(V) of up to 160 and 105  $\text{mg g}^{-1}$ , respectively. This exceptional As adsorption reactivity makes GR a potentially novel and environmentally-relevant mineral substrate for the sequestration of As in reduced groundwater systems. The removal of As is also highly pH dependent – high As(III) removal was obtained at higher pH while As(V) removal was found to be more favorable at circum-neutral conditions.  $GR_{SO_4}$  exhibited fast As uptake rates at alkaline conditions. Common groundwater species such as  $Mg^{2+}$  and  $PO_4^{3-}$  were found to affect the efficiency of As adsorption onto  $GR_{SO_4}$ . Overall, our results clearly highlight importance of redox-active GR mineral phases



in removing As species from aqueous solutions and their potential crucial role in the remediation of contaminated groundwaters.

## Acknowledgement

This project has received funding from the European Union's Horizon 2020 Marie Skłodowska-Curie Innovative Training Network Grant No. 675219 for JPHP and LGB and the German Helmholtz Recruiting Initiative (award number I-044-16-01) funding to LGB and HMF. ICP-OES analyses were carried out at the Helmholtz Laboratory for the Geochemistry of the Earth Surface (HELGES), GFZ Potsdam. We thank Rogier Besselink from the Interface Geochemistry Section at GFZ for the help with the BET analyses; Andrea Vieth-Hillebrand from the Organic Geochemistry Section at GFZ for the help with ion chromatography analysis; and Andy P. Brown from the Leeds Electron Microscopy and Spectroscopy Centre (LEMAS), University of Leeds, for the help with electron diffraction and EDX mapping, and for providing reference EEL spectra for hedenbergite and hematite samples. We also acknowledge the help of Jörg Radnik from the German Federal Institute for Materials Research and Testing (BAM) with the XPS analyses and of Peter Adler from the Max Planck Institute for Chemical Physics of Solids for the Mössbauer analysis. XRD analyses were done with the assistance of Marco C. Mangayayam and Dominique J. Tobler from NanoGeoScience, University of Copenhagen. The authors would also like to thank Robin Wojcik of the Interface Geochemistry Section at GFZ for his help in the graphical abstract.

## Appendix A. Supplementary data

Details on mineral characterization and data (XRD, TEM, SAED, EDX, EELS, N<sub>2</sub> sorption, XPS, Mössbauer spectroscopy, ICP-OES, ion chromatography), batch adsorption experimental methods and data and aqueous concentration analysis of long-term batch experiments can be found in the Supporting Information. Supplementary data associated with this article can be found in the online version. <https://doi.org/10.1016/j.scitotenv.2018.08.163>

## References

- Ahmed, I.A.M., Shaw, S., Benning, L.G., 2008. Formation of hydroxysulphate and hydroxycarbonate green rusts in the presence of zinc using time-resolved *in situ* small and wide angle X-ray scattering. *Mineral. Mag.* 72, 159–162.
- Ahmed, I.A.M., Benning, L.G., Kakonyi, G., Sumoondur, A.D., Terrill, N.J., Shaw, S., 2010. Formation of green rust sulfate: a combined *in situ* time-resolved X-ray scattering and electrochemical study. *Langmuir* 26, 6593–6603.
- Asere, T.G., De Clercq, J., Verbeke, K., Tessema, D.A., Fufa, F., Stevens, C.V., Du Laing, G., 2017. Uptake of arsenate by aluminum (hydr)oxide coated red scoria and pumice. *Appl. Geochem.* 78, 83–95.
- Bocher, F., Géhin, A., Ruby, C., Ghanbaja, J., Abdelmoula, M., Génin, J.-M.R., 2004. Coprecipitation of Fe(II–III) hydroxycarbonate green rust stabilised by phosphate adsorption. *Solid State Sci.* 6, 117–124.
- Bostick, B.C., Fendorf, S., 2003. Arsenite sorption on troilite (FeS) and pyrite (FeS<sub>2</sub>). *Geochim. Cosmochim. Acta* 67, 909–921.
- Brinza, L., Vu, H.P., Shaw, S., Mosselmans, J.F.W., Benning, L.G., 2015. Effect of Mo and V on the hydrothermal crystallization of hematite from ferrihydrite: an *in situ* energy dispersive X-ray diffraction and X-ray absorption spectroscopy study. *Cryst. Growth Des.* 15, 4768–4780.
- Brown, A.P., Hillier, S., Brydson, R.M.D., 2017. Quantification of Fe-oxidation state in mixed valence minerals: a geochemical application of EELS revisited. *J. Phys. Conf. Ser.* 902, 012016.
- Burton, E.D., Bush, R.T., Sullivan, L.A., Mitchell, D.R.G., 2008. Schwertmannite transformation to goethite via the Fe(II) pathway: reaction rates and implications for iron-sulfide formation. *Geochim. Cosmochim. Acta* 72, 4551–4564.
- Burton, E.D., Bush, R.T., Johnston, S.G., Watling, K.M., Hocking, R.K., Sullivan, L.A., Parker, G.K., 2009. Sorption of arsenic(V) and arsenic(III) to schwertmannite. *Environ. Sci. Technol.* 43, 9202–9207.
- Christiansen, B.C., Balic-Zunic, T., Petit, P.O., Frandsen, C., Mørup, S., Geckeis, H., Katerinopoulou, A., Stipp, S.L.S., 2009. Composition and structure of an iron-bearing, layered double hydroxide (LDH) – green rust sodium sulphate. *Geochim. Cosmochim. Acta* 73, 3579–3592.
- Christiansen, B.C., Geckeis, H., Marquardt, C.M., Bauer, A., Römer, J., Wiss, T., Schild, D., Stipp, S.L.S., 2011. Neptunyl (Np) interaction with green rust. *Geochim. Cosmochim. Acta* 75, 1216–1226.
- Cundy, A.B., Hopkinson, L., Whitby, R.L.D., 2008. Use of iron-based technologies in contaminated land and groundwater remediation: a review. *Sci. Total Environ.* 400, 42–51.
- Davidson, L.E., Shaw, S., Benning, L.G., 2008. The kinetics and mechanisms of schwertmannite transformation to goethite and hematite under alkaline conditions. *Am. Mineral.* 93, 1326.
- de Roy, A., Forano, C., Besse, J.P., 2001. Layered double hydroxides: synthesis and post-synthesis modification. In: Rives, V. (Ed.), *Layered Double Hydroxides: Present and Future*. Nova Science Publishers, New York, pp. 1–39.
- Ferguson, J.F., Gavis, J., 1972. A review of the arsenic cycle in natural waters. *Water Res.* 6, 1259–1274.
- Folens, K., Leus, K., Nicomel, N.R., Meledina, M., Turner, S., Van Tendeloo, G., Laing, G.D., Van Der Voort, P., 2016. Fe<sub>3</sub>O<sub>4</sub>@MIL-101 – a selective and regenerable adsorbent for the removal of As species from water. *Eur. J. Inorg. Chem.* 4395–4401.
- Géhin, A., Ruby, C., Abdelmoula, M., Benali, O., Ghanbaja, J., Refait, P., Génin, J.-M.R., 2002. Synthesis of Fe(II–III) hydroxysulphate green rust by coprecipitation. *Solid State Sci.* 4, 61–66.
- Génin, J.-M.R., Ruby, C., 2004. Anion and cation distributions in Fe(II–III) hydroxysalt green rusts from XRD and Mössbauer analysis (carbonate, chloride, sulphate, ...); the “fougerite” mineral. *Solid State Sci.* 6, 705–718.
- Goh, K.-H., Lim, T.-T., Dong, Z., 2008. Application of layered double hydroxides for removal of oxyanions: a review. *Water Res.* 42, 1343–1368.
- Guilbaud, R., White, M.L., Poulton, S.W., 2013. Surface charge and growth of sulphate and carbonate green rust in aqueous media. *Geochim. Cosmochim. Acta* 108, 141–153.
- Guo, X., Chen, F., 2005. Removal of arsenic by bead cellulose loaded with iron oxyhydroxide from groundwater. *Environ. Sci. Technol.* 39, 6808–6818.
- Gupta, A., Chauhan, V.S., Sankaramakrishnan, N., 2009. Preparation and evaluation of iron–chitosan composites for removal of As(III) and As(V) from arsenic contaminated real life groundwater. *Water Res.* 43, 3862–3870.
- Ho, Y.-S., 2006. Review of second-order models for adsorption systems. *J. Hazard. Mater.* 136, 681–689.
- Hongshao, Z., Stanforth, R., 2001. Competitive adsorption of phosphate and arsenate on goethite. *Environ. Sci. Technol.* 35, 4753–4757.
- Hughes, M.F., 2002. Arsenic toxicity and potential mechanisms of action. *Toxicol. Lett.* 133, 1–16.
- Inskeep, W.P., McDermott, T.R., Fendorf, S., 2002. Arsenic (V)/(III) recycling in soils and natural waters: chemical and microbiological processes. In: Frankenberger, W.T. (Ed.), *Environmental Chemistry of Arsenic*. Marcel Dekker, New York, pp. 183–215.
- Jain, A., Raven, K.P., Loeppert, R.H., 1999. Arsenite and arsenate adsorption on ferrihydrite: surface charge reduction and net OH<sup>-</sup> release stoichiometry. *Environ. Sci. Technol.* 33, 1179–1184.
- Jönsson, J., Sherman, D.M., 2008. Sorption of As(III) and As(V) to siderite, green rust (fougerite) and magnetite: implications for arsenic release in anoxic groundwaters. *Chem. Geol.* 255, 173–181.
- Lenoble, V., Bouras, O., Deluchat, V., Serpaud, B., Bollinger, J.-C., 2002. Arsenic adsorption onto pillared clays and iron oxides. *J. Colloid Interface Sci.* 255, 52–58.
- Leus, K., Perez, J.P.H., Folens, K., Meledina, M., Van Tendeloo, G., Du Laing, G., Van Der Voort, P., 2017. UiO-66-(SH)<sub>2</sub> as stable, selective and regenerable adsorbent for the removal of mercury from water under environmentally-relevant conditions. *Faraday Discuss.* 201, 145–161.
- Leus, K., Folens, K., Nicomel, N.R., Perez, J.P.H., Filippousi, M., Meledina, M., Dîrtu, M.M., Turner, S., Van Tendeloo, G., Garcia, Y., Du Laing, G., Van Der Voort, P., 2018. Removal of arsenic and mercury species from water by covalent triazine framework encapsulated  $\gamma$ -Fe<sub>2</sub>O<sub>3</sub> nanoparticles. *J. Hazard. Mater.* 353, 312–319.
- Lightstone, F.C., Schwegler, E., Hood, R.Q., Gygi, F., Galli, G., 2001. A first principles molecular dynamics simulation of the hydrated magnesium ion. *Chem. Phys. Lett.* 343, 549–555.
- Limousin, G., Gaudet, J.P., Charlet, L., Szenknect, S., Barthès, V., Krmissa, M., 2007. Sorption isotherms: a review on physical bases, modeling and measurement. *Appl. Geochem.* 22, 249–275.
- Lin, S., Lu, D., Liu, Z., 2012. Removal of arsenic contaminants with magnetic  $\gamma$ -Fe<sub>2</sub>O<sub>3</sub> nanoparticles. *Chem. Eng. J.* 211–212, 46–52.
- Malis, T., Cheng, S.C., Egerton, R.F., 1988. EELS log-ratio technique for specimen-thickness measurement in the TEM. *J. Electron Microsc. Tech.* 8, 193–200.
- Masscheleyn, P.H., Delaune, R.D., Patrick, W.H., 1991. Arsenic and selenium chemistry as affected by sediment redox potential and pH. *J. Environ. Qual.* 20, 522–527.
- Mitsunobu, S., Takahashi, Y., Sakai, Y., Inumaru, K., 2009. Interaction of synthetic sulfate green rust with antimony(V). *Environ. Sci. Technol.* 43, 318–323.
- Miyata, S., 1983. Anion-exchange properties of hydrotalcite-like compounds. *Clay Clay Miner.* 31, 305–311.
- Mullet, M., Guillemin, Y., Ruby, C., 2008. Oxidation and deprotonation of synthetic Fe<sup>II</sup>-Fe<sup>III</sup> (oxy)hydroxycarbonate Green Rust: an X-ray photoelectron study. *J. Solid State Chem.* 181, 81–89.
- Nedel, S., Dideriksen, K., Christiansen, B.C., Bovet, N., Stipp, S.L.S., 2010. Uptake and release of cerium during Fe-oxide formation and transformation in Fe(II) solutions. *Environ. Sci. Technol.* 44, 4493–4498.
- Nickson, R.T., McArthur, J.M., Ravenscroft, P., Burgess, W.G., Ahmed, K.M., 2000. Mechanism of arsenic release to groundwater, Bangladesh and West Bengal. *Appl. Geochem.* 15, 403–413.
- O’Loughlin, E.J., Kelly, S.D., Cook, R.E., Csencsits, R., Kemner, K.M., 2003. Reduction of uranium(VI) by mixed iron(II)/iron(III) hydroxide (green rust): formation of UO<sub>2</sub> nanoparticles. *Environ. Sci. Technol.* 37, 721–727.
- Ona-Nguema, G., Morin, G., Wang, Y., Menguy, N., Juillot, F., Olivi, L., Aquilanti, G., Abdelmoula, M., Ruby, C., Bargar, J.R., Guyot, F., Calas, G., Brown, G.E., 2009. Arsenite sequestration at the surface of nano-Fe(OH)<sub>2</sub>, ferrous-carbonate hydroxide, and green-rust after bioreduction of arsenic-sorbed lepidocrocite by *Shewanella putrefaciens*. *Geochim. Cosmochim. Acta* 73, 1359–1381.

- Randall, S.R., Sherman, D.M., Ragnarsdottir, K.V., 2001. Sorption of As(V) on green rust ( $\text{Fe}_4(\text{II})\text{Fe}_2(\text{III})(\text{OH})_{12}\text{SO}_4 \cdot 3\text{H}_2\text{O}$ ) and lepidocrocite ( $\gamma\text{-FeOOH}$ ): surface complexes from EXAFS spectroscopy. *Geochim. Cosmochim. Acta* 65, 1015–1023.
- Raven, K.P., Jain, A., Loeppert, R.H., 1998. Arsenite and arsenate adsorption on ferrihydrite: kinetics, equilibrium, and adsorption envelopes. *Environ. Sci. Technol.* 32, 344–349.
- Refait, P., Bauer, P., Olowe, A.A., Génin, J.M.R., 1990. The substitution of  $\text{Fe}^{2+}$  ions by  $\text{Ni}^{2+}$  ions in the green rust 2 compound studied by Mössbauer effect. *Hyperfine Interact.* 57, 2061–2066.
- Refait, P., Simon, L., Génin, J.-M.R., 2000. Reduction of  $\text{SeO}_4^{2-}$  anions and anoxic formation of iron(II)–iron(III) hydroxy-selenate green rust. *Environ. Sci. Technol.* 34, 819–825.
- Roberts, L.C., Hug, S.J., Ruettimann, T., Billah, M.M., Khan, A.W., Rahman, M.T., 2004. Arsenic removal with iron(II) and iron(III) in waters with high silicate and phosphate concentrations. *Environ. Sci. Technol.* 38, 307–315.
- Schuessler, J.A., Kämpf, H., Koch, U., Alawi, M., 2016. Earthquake impact on iron isotope signatures recorded in mineral spring water. *J. Geophys. Res. Solid Earth* 121, 8548–8568.
- Sharma, V.K., Sohn, M., 2009. Aquatic arsenic: toxicity, speciation, transformations, and remediation. *Environ. Int.* 35, 743–759.
- Shipley, H.J., Yean, S., Kan, A.T., Tomson, M.B., 2009. Adsorption of arsenic to magnetite nanoparticles: effect of particle concentration, pH, ionic strength, and temperature. *Environ. Toxicol. Chem.* 28, 509–515.
- Simon, L., François, M., Refait, P., Renaudin, G., Lelaurain, M., Génin, J.-M.R., 2003. Structure of the Fe(II-III) layered double hydroxysulphate green rust two from Rietveld analysis. *Solid State Sci.* 5, 327–334.
- Skovbjerg, L.L., Stipp, S.L.S., Utsunomiya, S., Ewing, R.C., 2006. The mechanisms of reduction of hexavalent chromium by green rust sodium sulphate: formation of Cr-goethite. *Geochim. Cosmochim. Acta* 70, 3582–3592.
- Smedley, P.L., Kinniburgh, D.G., 2002. A review of the source, behaviour and distribution of arsenic in natural waters. *Appl. Geochem.* 17, 517–568.
- Su, C., Puls, R.W., 2004. Significance of iron(II,III) hydroxycarbonate green rust in arsenic remediation using zerovalent iron in laboratory column tests. *Environ. Sci. Technol.* 38, 5224–5231.
- Su, C., Wilkin, R.T., 2005. Arsenate and arsenite sorption on and arsenite oxidation by iron (II, III) hydroxycarbonate green rust. *Advances in Arsenic Research*. 915. American Chemical Society, pp. 25–40.
- Tang, W., Li, Q., Gao, S., Shang, J.K., 2011. Arsenic (III,V) removal from aqueous solution by ultrafine  $\alpha\text{-Fe}_2\text{O}_3$  nanoparticles synthesized from solvent thermal method. *J. Hazard. Mater.* 192, 131–138.
- Usman, M., Byrne, J.M., Chaudhary, A., Orsetti, S., Hanna, K., Ruby, C., Kappler, A., Haderlein, S.B., 2018. Magnetite and green rust: synthesis, properties, and environmental applications of mixed-valent iron minerals. *Chem. Rev.* 118, 3251–3304.
- Vaughan, D.J., 2006. Arsenic. *Elements* 2, 71–75.
- Vu, H.P., Shaw, S., Brinza, L., Benning, L.G., 2013. Partitioning of Pb(II) during goethite and hematite crystallization: implications for Pb transport in natural systems. *Appl. Geochem.* 39, 119–128.
- Wang, Y., Morin, G., Ona-Nguema, G., Juillot, F., Guyot, F., Calas, G., Brown, G.E., 2010. Evidence for different surface speciation of arsenite and arsenate on green rust: an EXAFS and XANES study. *Environ. Sci. Technol.* 44, 109–115.
- Wang, Y., Morin, G., Ona-Nguema, G., Brown, G.E., 2014. Arsenic(III) and arsenic(V) speciation during transformation of lepidocrocite to magnetite. *Environ. Sci. Technol.* 48, 14282–14290.
- Williams, M., Fordyce, F., Pajitrapaporn, A., Charoenchaisri, P., 1996. Arsenic contamination in surface drainage and groundwater in part of the southeast Asian tin belt, Nakhon Si Thammarat Province, southern Thailand. *Environ. Geol.* 27, 16–33.
- Wolthers, M., Charlet, L., van Der Weijden, C.H., van der Linde, P.R., Rickard, D., 2005. Arsenic mobility in the ambient sulfidic environment: sorption of arsenic(V) and arsenic(III) onto disordered mackinawite. *Geochim. Cosmochim. Acta* 69, 3483–3492.
- World Health Organization, 2017. *Guidelines for Drinking-water Quality: Fourth edition Incorporating the First Addendum*. (Geneva).
- Yean, S., Cong, L., Yavuz, C.T., Mayo, J.T., Yu, W.W., Kan, A.T., Colvin, V.L., Tomson, M.B., 2005. Effect of magnetite particle size on adsorption and desorption of arsenite and arsenate. *J. Mater. Res.* 20, 3255–3264.
- Yee, N., Shaw, S., Benning, L.G., Nguyen, T.H., 2006. The rate of ferrihydrite transformation to goethite via the Fe(II) pathway. *Am. Mineral.* 91, 92–96.
- Zahid, A., Hassan, M.Q., Balke, K.D., Flegler, M., Clark, D.W., 2008. Groundwater chemistry and occurrence of arsenic in the Meghna floodplain aquifer, southeastern Bangladesh. *Environ. Geol.* 54, 1247–1260.